Engineering xxx (xxxx) xxx

Contents lists available at ScienceDirect

Engineering

journal homepage: www.elsevier.com/locate/eng

Research
Medical Engineering—Article

Enhanced Precision Therapy of Multiple Myeloma Through Engineered Biomimetic Nanoparticles with Dual Targeting

Ruogu Qi [a,#,*], Shanshan Wang [a,b,#], Jiayi Yu [c,#], Tianming Lu [a], Zhiqiang Bi [a], Weibo Liu [d], Yuanyuan Guo [a], Yong Bian [b], Jianliang Shen [e,*], Xuesong Zhang [d,*], Wenhao Hu [d,*]

[a] School of Medicine, Nanjing University of Chinese Medicine, Nanjing 210023, China
[b] Laboratory Animal Center, Nanjing University of Chinese Medicine, Nanjing 210023, China
[c] Key Laboratory of Carcinogenesis and Translational Research, Ministry of Education/Beijing, Department of Radiation Oncology, Beijing Cancer Hospital, Beijing 100142, China
[d] Department of Orthopedics, The Fourth Medical Center, The Chinese People's Liberation Army General Hospital, Beijing 100853, China
[e] State Key Laboratory of Ophthalmology, Optometry and Vision Science, School of Biomedical Engineering, Wenzhou Medical University, Wenzhou 325027, China

ARTICLE INFO

Article history:
Received 25 October 2023
Revised 6 December 2023
Accepted 2 January 2024
Available online 17 January 2024

Keywords:
Multiple myeloma
Bortezomib
Drug delivery
Dual targeting
Controlled release

ABSTRACT

Multiple myeloma (MM) is the second most prevalent hematological malignancy. Current MM treatment strategies are hampered by systemic toxicity and suboptimal therapeutic efficacy. This study addressed these limitations through the development of a potent MM-targeting chemotherapy strategy, which capitalized on the high binding affinity of alendronate for hydroxyapatite in the bone matrix and the homologous targeting of myeloma cell membranes, termed T-PB@M. The results from our investigations highlight the considerable bone affinity of T-PB@M, both *in vitro* and *in vivo*. Additionally, this material demonstrated a capability for drug release triggered by low pH conditions. Moreover, T-PB@M induced the generation of reactive oxygen species and triggered cell apoptosis through the poly(ADP-ribose) polymerase 1 (PARP1)–Caspase-3–B-cell lymphoma-2 (Bcl-2) pathway in MM cells. Notably, T-PB@M preferentially targeted bone-involved sites, thereby circumventing systemic toxic side effects and leading to prolonged survival of MM orthotopic mice. Therefore, this designed target-MM nanocarrier presents a promising and potentially effective platform for the precise treatment of MM.

1. Introduction

Multiple myeloma (MM) is a prevalent hematological malignancy affecting adults and is the second most frequently diagnosed form of such cancers globally [1–3]. The disease manifests through the aberrant conversion and unregulated clonal expansion of malignant plasma cells in the bone marrow. These excessively proliferative malignant plasma cells can outpace normal plasma cells, which leads to the disruption of bone integrity and suppression of hematopoiesis [4,5]. Progressive symptoms include bone pain, anemia, renal dysfunction, and susceptibility to infections [6,7]. In addition, complications, such as amyloidosis may arise [8,9]. Consequently, patients with MM are rarely curable, which has led to a notable rise in mortality rates and a significant deterioration in patients' quality of life.

Current approaches in the clinical management of MM include autologous stem cell transplant and immunotherapy [10,11]. However, chemotherapy has retained its significance because of its indispensability in combination with novel treatments. Bortezomib (BTZ), the pioneering proteasome inhibitor approved for clinical use, stands as a first-line therapy for MM [12,13]. BTZ exhibits selective binding to the active site of the proteasome, thereby impeding its function. Consequently, the normal metabolic processes and protein degradation within cancer cells are compromised, culminating in cancer cell apoptosis [14,15]. Furthermore, BTZ also modulates various signaling pathways, including nuclear factor kappa B (NF-κB), phosphoinositide-3-kinase(PI3K)/protein kinase B (Akt) signaling pathway, and Janus kinase(JAK)/signal transducer and activator of transcription (STAT) pathways, thereby exerting influence over cancer cell proliferation, metastasis, drug resistance, and other biological behaviors [16–18]. Despite its ability to induce durable remission and extend overall survival, BTZ

* Corresponding authors.
E-mail addresses: rqi@njucm.edu.cn (R. Qi), shenjl@wiucas.ac.cn (J. Shen), zhangxuesong301@126.com (X. Zhang), luckyhao555@163.com (W. Hu).
# These authors contributed equally to this work.

https://doi.org/10.1016/j.eng.2024.01.001

Please cite this article as: R. Qi, S. Wang, J. Yu et al., Enhanced Precision Therapy of Multiple Myeloma Through Engineered Biomimetic Nanoparticles with Dual Targeting, Engineering, https://doi.org/10.1016/j.eng.2024.01.001

still falls short of providing a cure for patients with MM. The primary obstacle lies in the challenge of delivering a therapeutically effective quantity of BTZ to the principal site of MM, thereby impeding the eradication of MM cells residing within the bone marrow. Moreover, clinical application of highly toxic BTZ is accompanied by several toxic side effects, including peripheral neuropathy, leukopenia, potential agranulocytosis, and severe organ damage [19,20]. Consequently, the ability to innovate and create a novel targeted drug delivery system capable of promoting optimal drug transport to the bone marrow, selectively targeting MM cells, and mitigating adverse effects is urgently needed.

To optimize the therapeutic efficacy of BTZ while minimizing its systemic toxicity, diverse strategies have been employed. These include the development of polymer-drug conjugates or the utilization of various carrier systems, such as micelles, liposomes, and nanoparticles [21–24]. Advanced delivery systems for BTZ often capitalize on environmentally triggered mechanisms, such as exploiting the slightly lower extracellular pH in tumor tissue compared with normal tissue, which enables precise pH-triggered drug release at the tumor site. The heightened acidity within subcellular compartments, notably the endosome, provides an additional avenue to enhance the efficacy of anticancer drug delivery through pH-initiated release from endocytosed drug carriers [25]. Thus, nanoformulations of BTZ have demonstrated improved efficacy and reduced side effects in the treatment of solid tumors. Nevertheless, in the context of hematological malignancies, particularly MM, the enhanced permeability and retention (EPR) effect has exhibited diminished prominence compared with solid tumors [26,27]. Hematomas possess a distinct vascular structure and tumor tissue characteristics, thereby limiting the impact of the EPR effect in this context. To enhance the targeting capability of drug-loaded nanoparticles toward hematological malignancy cells, recent attention has been drawn toward biomimetic nanoparticles coated by cell membranes, as the membrane coating can effectively retain the targeting properties of the original cell type [28,29]. By preserving the specific surface markers or receptors of cancer cells, cancer cell membrane-coated nanoparticles enable selective targeting of tumor tissues. As a result, they can promote nanoparticle accumulation at the desired site and improve drug delivery to tumor cells [30]. In the context of MM cells, their survival and proliferation largely depend on their ability to migrate and reestablish within the bone marrow microenvironment, a phenomenon referred to as "bone marrow homing" [31,32]. Bone marrow homing occurs throughout the development of MM. Hence, it has been postulated that through the utilization of the distinctive attributes of cancer cell membrane-coated nanoparticles and the inherent characteristics of bone marrow homing in MM cells, the development of nanoparticles coated with MM cell membranes could enhance the effective delivery of therapeutic agents to the bone marrow region. This approach aims to optimize the nanoparticle–cell interactions through homotypic targeting, thereby augmenting the therapeutic efficacy and achieving favorable treatment outcomes. Although the cancer cell membrane coating enhances biocompatibility, concerns persist regarding immune system recognition and clearance. The immune system's identification of the cancer cell membrane coating as foreign may trigger an immune response that could compromise the nanoparticles' efficacy or neutralize them altogether. Furthermore, considering the bone marrow localization of MM, targeting the tumor cells alone using the myeloma cell membrane is insufficient. It is imperative to bolster the bone-targeting capacity of nanoparticles to facilitate effective BTZ delivery to the bone marrow, thus mitigating systemic toxicity and optimizing therapeutic outcomes.

The bisphosphonate named alendronate (ALN), which is endorsed by the US Food and Drug Administration for postmenopausal osteoporosis therapy, possesses the capability to bind with calcium phosphate within bone structure [33,34]. Because of its remarkable bone-targeting characteristics, ALN is currently under investigation as a promising carrier for drug delivery to bone and bone marrow to impede bone resorption and decelerate the progression of osteoporosis. Additionally, the combined administration of ALN and BTZ exhibits synergistic effects, whereby the two drugs complement each other, resulting in enhanced treatment efficacy and decreased occurrence of MM [35,36]. Nevertheless, despite the potential advantages of combining BTZ and ALN for targeted drug delivery to bone under acidic conditions, the limited ability to selectively target tumor cells impedes their practicality in the treatment of MM.

In this study, a potent MM-targeting chemotherapeutic strategy by harnessing the high binding affinity of ALN in the bone matrix with the homologous targeting of myeloma cell membranes was developed. First, a star-shape biodegradable polyaspartamide with catechol caffeic acid (CA) conjugation was prepared (denoted as P1). Subsequently, P1 with catechol pendant can be used to conjugate BTZ via acidic-sensitivity borate ester to form nanoparticles (denoted as PB). Then, MM cell membranes and ALN containing lipid were encapsulated with PB into BTZ composite MM-targeting nanoparticles (denoted as T-PB@M) (Fig. 1).

It is hypothesized that T-PB@M could penetrate into the bone cavity due to the bone-binding affinity of ALN, and then augment MM cellular uptake through bone marrow homing targeting. Furthermore, the bone-targeting nanoparticles could ensure the *in vivo* stability of the carrier-bound potent BTZ, thereby preventing premature release and reducing side effects. Consequently, this innovative strategy may hold promise for achieving improved therapeutic efficacy in the treatment of MM.

2. Materials and methods

2.1. Materials and reagents

BTZ, 1,2-distearoyl-*sn*-glycero-3-phosphoethanolamine–*N*-[methoxy(polyethylene glycol)-2000]–*N*-hydroxysuccinimide (DSPE–PEG_{2000}–NHS), 3-(4,5-dimethyl-2-thiazolyl)-2,5-diphenyltetrazolium bromide salt (MTT), tetraethylenepentamine, generation 0 polyamidoamine dendrimer (G0 PAMAM), fluorescein isothiocyanate (FITC), and IR780 iodide were obtained from Shanghai Macklin Biochemical Co., Ltd. (China); nanosize hydroxyapatite (HAP) were purchased from Shanghai Aladdin Biochemical Technology Co., Ltd. (China); β-benzyl-*L*-aspartate (Bzl-Asp) and triphosgene were purchased from GL Biochem (Shanghai) Ltd. (China). The *N*-carboxy anhydride (NCAs) of Bzl-Asp according to a similar method described in Ref. [37]. The 2′,7′-dichlorofluorescein diacetate (DCFH-DA) Detection Kit were purchased from Beyotime Biotech Inc. (China). Annexin V/propidium iodide (PI) Apoptosis Detection Kit was obtained from Vazyme Biotech Co., Ltd. (China). Poly (ADP-ribose) polymerase 1 (PARP1), Caspase-3, and B-cell lymphoma-2 (Bcl-2) antibodies were purchased from Cell Signaling Technology, Inc. (USA) for Western blot analysis. All other reagents were used directly without further purification. Fetal bovine serum (FBS), Roswell Park Memorial Institute (RPMI) 1640 medium, penicillin, and streptomycin were obtained from Thermo Fisher Scientific Inc. (USA). Serum alanine aminotransferase (ALT), aspartate aminotransferase (AST), blood urea nitrogen (BUN), serum creatinine (CREA), hemoglobin, serum calcium, and urine protein were purchased from Nanjing Jiancheng Bioengineering Engineering Institute (China); immunoglobulin G was purchased from Enzyme-Linked Biotechnology Co., Ltd. (China).

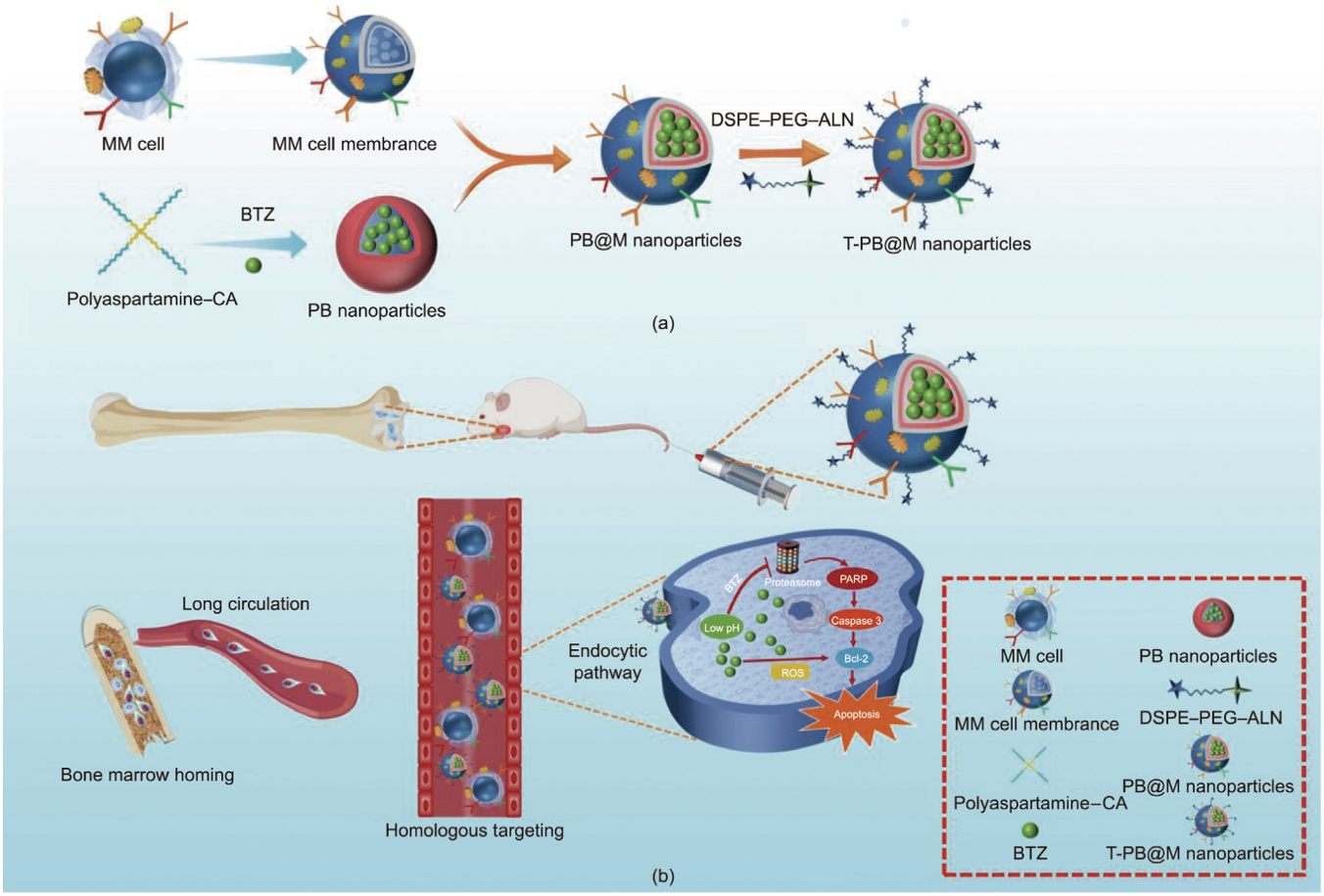

Fig. 1. Scheme of T-PB@M nanoparticles for treatment of MM. (a) Schematic diagram of the preparation process of T-PB@M. (b) Schematic mechanism of T-PB@M after intravenous administration. DSPE–PEG: 1,2-distearoyl-*sn*-glycero-3-phosphoethanolamine–polyethylene glycol; ROS: reactive oxygen species; PARP: poly(ADP-ribose) polymerase 1; Bcl-2: B-cell lymphoma-2.

2.2. Cell line

Human MM cell lines (U266 and MM.1S) were purchased from the cell bank of the Chinese Academy of Sciences (China). Cells were incubated in the media of RPMI 1640 contained 10% FBS and 1% penicillin/streptomycin. The cell lines were incubated in an incubator at 37 °C containing 5% CO_2.

2.3. Animals

NCG (NOD/ShiLtJGpt-Prkdcem26Cd52Il2rgem26Cd22/Gpt) mice, BALB/C-nu/nu mice, and ICR mice (5–6 weeks) were provided by GemPharmatech Co., Ltd. (China). All experimental procedures were performed in accordance with the procedures approved by the Animal Care and Use Committee of Nanjing University of Chinese Medicine (ethics No. 202307A007). All mice were maintained under specific pathogen-free (SPF) conditions at the Laboratory Animal Center of Nanjing University of Chinese Medicine.

2.4. Synthesis of T-PB@M

2.4.1. Synthesis of star-shaped polyaspartamine

Star-shaped polyaspartamine was prepared via G0 PAMAM-initiated ring-opening polymerization (ROP) of Bzl-Asp–NCA in dimethyl sulfoxide (DMSO) by ammonolysis of tetraethylenepentamine as reported in Ref. [38].

2.4.2. Synthesis of polyaspartamine–CA

Typically, 100 mg of polyaspartamine, 35 mg of CA, 50 mg of 1-ethyl-3-(3-dimethylamino) propyl carbodiimide hydrochloride (EDC), and 60 mg of NHS were dissolvedin 10 mL of DMSO and stirred at 4 °C for 24 h. The resultant solution was placed into a dialysis bag (molecular weight cut-off (MWCO) = 3500 Da) and dialyzed against water for 48 h (which was changed every 4 h) to remove unreacted materials and by-products. Then the solution of polyaspartamine–CA conjugation was lyophilized for further use. The synthetic was characterized by ^{1}H nuclear magnetic resonance (NMR) spectra at 400 MHz on a Bruker 400 Avance III (Germany) instrument.

2.4.3. Synthesis of DSPE–PEG–ALN

DSPE–PEG–NHS (100.0 mg, 0.1 mmol) and ALN (32.0 mg, 0.2 mmol) were dissolved in 40.0 mL of purified water. Then the solution was stirred for one day at 25 °C, which was dialyzed (MWCO = 1000 Da) against water for 3 d and lyophilized to obtain a white solid DSPE–PEG–ALN.

2.4.4. Cell membrane isolation

Firstly, MM cells were harvested and suspended in a hypotonic lysing buffer consisting of 20 mmol·L^{-1} Tris-HCl (pH = 7.4), 10 mmol·L^{-1} KCl, 2 mmol·L^{-1} $MgCl_2$, and an ethylenediaminetetraacetic acid (EDTA)-free mini-protease inhibitor tablet per 10 mL of solution. The entire cell suspension was then disrupted

by passing it through a Dounce homogenizer for 20 cycles. After homogenization, the supernatant was collected by centrifugation at 3200*g* (1*g* = 9.8 $m \cdot s^{-2}$) for 5 min. The pellet resulting from the initial centrifugation was resuspended in the hypotonic lysing buffer, and the previously noted steps were repeated twice. The supernatants obtained from each round of centrifugation were combined and subjected to further centrifugation at 12 000*g* for 30 min. The resulting supernatant was washed once with a solution containing 10 $mmol \cdot L^{-1}$ Tris-HCl (pH = 7.4) and 1 $mmol \cdot L^{-1}$ EDTA. Finally, the purified MM cell membrane was collected and used for subsequent experiments. Following the method of membrane extraction above, the samples are lyophilized and weighed. A total 850 μg of membrane was extracted from 1×10^7 U266 cells for subsequent experiments.

2.4.5. Synthesis of PB

BTZ (10.7 mg, 0.2 mL) was dissolved in DMSO, the solution (100 mg, 10 mL) of polyaspartamine–CA in H_2O was added to the above DMSO solution, and the mixture was stirred for 15 min at room temperature. Subsequently, phosphate-buffered saline (PBS) buffer (20 mL, pH = 7.4) was added with gentle agitation for 2 h to allow the complete interaction between BTZ and the catechol-containing polymer. The nonconjugated BTZ and residual solvent were dialyzed (MWCO = 3500 Da) against water for three days and lyophilized to yield a yellowish powder. The BTZ content in the PB was quantified using high-performance liquid chromatography (HPLC) analysis.

2.4.6. Synthesis of PB@M

The MM cell membrane was first physically extruded through a 200 nm polycarbonate membrane for ten passes to obtain the MM vesicles (MMs). Next, the PB nanoparticles and the MMs were mixed and then sequentially extruded through a polycarbonate membrane with pore sizes of 200 nm to prepare the PB@M nanoparticles.

2.4.7. Synthesis of T-PB@M

To prepare the T-PB@M nanoparticles, PB@M (2 mg, 10 mL) and DSPE–PEG–ALN (2 mg, 10 mL) were dissolved in water and mixed. The mixture was sequentially extruded through a polycarbonate membrane with pore sizes of 200 nm. This process resulted in the formation of the final T-PB@M nanoparticles.

2.5. Synthesis of FITC-labeled PB

Typically, 2 mg of PB, 0.1 mg of FITC, 1 mg of EDC, and 1 mg of NHS were dissolved in 10 mL of DMSO and stirred at 4 °C for 24 h. Subsequently, the resultant solution was dialyzed (MWCO = 3500 Da) against water for 3 d and lyophilized for subsequent experiments.

2.6. Synthesis of IR780-labeled PB

To prepare the IR780-labeled PB, firstly, the carboxyl derivative of IR780 (IR780-COOH) was synthesized as reported in Refs. [39–41]. Then, the synthesis of IR780-PB was performed as FITC-PB as described above.

2.7. Sodium dodecyl-sulfate polyacrylamide gel electrophoresis (SDS-PAGE)

Briefly, the MM membrane, PB@M, and T-PB@M were mixed with 1× loading buffer and in a 100 °C metal bath for 5 min. Then the prepared protein samples were added to the acrylamide gel for SDS-PAGE in the BIO-RAD electrophoresis system. After 45 min, the gel was stained with 1× Coomassie Blue overnight and placed in the Gel Imager System for imaging after decolorization (ChemiDoc XRS+; BIO-RAD, USA).

2.8. In vitro *stability, hemolysis, and HAP-binding ability assay*

The stability of BTZ-NPs was evaluated in PBS buffer by monitoring the particle size at specific time points using dynamic light scattering (DLS) over a seven-day period. The alteration in particle size was employed as an indicator of the *in vitro* colloidal stability of the nanoparticles during the testing period.

For the hemolysis assay, fresh mouse/rabbit blood samples were used. PBS solution and pure water were used as the negative and positive controls, respectively. Whole blood samples were centrifuged at 3000 $r \cdot min^{-1}$ for 5 min and washed five times with PBS. Then, 0.25 mL of 4% (v/v) erythrocytes was mixed with 0.25 mL PBS containing free BTZ, PB, PB@M, and T-PB@M. The mixtures were incubated at 37 °C for 2 h and centrifuged at 500 $r \cdot min^{-1}$. The absorbance values of the supernatants at 545 nm were measured on a microplate reader after centrifugation. The percentage of hemolysis was calculated using the following equation:

$$\text{Hemolysis}(\%) = (H - H_C/H_0 - H_C) \times 100\% \quad (1)$$

where H represents the supernatant absorbance value of erythrocytes with free BTZ, PB, PB@M, and T-PB@M; H_0 represents the absorbance value of erythrocytes after complete hemolysis in pure water; and H_C represents the supernatant absorbance value of erythrocytes with PBS.

The HAP-binding ability assay was carried out by incubating FITC-labeled formulations with various ALN-containing samples in the presence of HAP at a quantity of 200 mg. The incubation process was conducted for 1 h at room temperature under gentle stirring conditions. After the incubation period, the HAP particles were separated by centrifugation. The absorbances of the supernatants were then measured by ultraviolet (UV)–visible spectra at the specific wavelength at 490 nm. The HAP hydroxyapatite was subsequently washed three times with PBS to remove any unbound particles and observed by fluorescence microscopy.

2.9. Drug-loading content and releasing assay

BTZ were analyzed using HPLC (e2695 series; Waters, USA) with a reverse phase C-18 column (Zorbax Eclipse XDB-C18, 4.6 mm × 150 mm; Agilent, USA). For the detection of BTZ, 35% acetonitrile solution in water containing 0.1% trifluoroacetic acid (TFA) was used as the mobile phase at a flow rate of 1 $mL \cdot min^{-1}$. Typically, 10 μL solution was injected and detected at retention time of 8.3 min, λ = 270 nm. The standard curve for BTZ was conducted at a BTZ concentration range of 0–200 $\mu g \cdot mL^{-1}$ ($y = 13.413x - 0.7409$, where x is the BTZ concentration, $\mu g \cdot mL^{-1}$, y is the peak area, $R^2 = 0.9999$). Drug-loading content (DL) was calculated as follows:

$$\text{DL} = W_T/W_{NP} \times 100\% \quad (2)$$

where W_T is the total mass of BTZ carried by the nanoparticles and W_{NP} is the overall mass of the nanoparticles. According to Eq. (2), DL was calculated to be 10%.

In vitro drug release was performed by an equilibrium dialysis method. The dialysis bags (MWCO = 3500 Da) containing the nanoparticles were introduced into the PBS solution with different pH (7.4, 6.5, 5.0) values at room temperature with a shaking speed of 500 $r \cdot min^{-1}$. At predetermined time points (1, 3, 6, 12, 24, and 48 h), the PBS was harvested and replaced with the same volume fresh PBS solution. The concentration of the BTZ was determined.

2.10. Cell cytotoxicity and cellular uptake

The cytotoxicity of free BTZ, PB, PB@M, and T-PB@M toward MM cells (U266 and MM.1S) were quantitatively detected using the MTT assay. Briefly, 1×10^4 U266 and MM.1S cells were seeded in a 96-well plate and free BTZ, PB, PB@M, and T-PB@M were added to the cells to achieve final serial BTZ concentrations of 5, 50, 100, 200, and 500 nmol·L^{-1}. The cells treated with PBS were used as the control. The plates were then incubated at 37 °C with 5% CO_2. After 24 and 48 h of incubation, the cell viability was assayed using the MTT method.

The cellular uptake of PB, PB@M, and T-PB@M were detected by flow cytometer (FCM) (Gallios; Beckman, USA) and fluorescent microscope (Axio Vert A1; Zeiss, Germany). Typically, U266 cells (1×10^5) were seeded in a 12-well plate and FITC-labeled PB, PB@M, and T-PB@M were added with the same concentration of the fluorescence, respectively. The cells in distinct groups were thoroughly washed with PBS three times and subjected to analysis via flow cytometry (FCM), where data were obtained from 15 000 cells per sample. Additionally, for a subsequent fluorescent imaging assay, the cells were fixed using a 4% paraformaldehyde solution after PBS washing, and the nuclei were stained with Hoechst for observation under a fluorescent microscope.

2.11. Cell apoptosis assay

Cell apoptosis induced by free BTZ, PB, PB@M, and T-PB@M therapy in U266 and MM.1S cells were investigated using the Annexin V-FITC/PI Apoptosis Detection Kit. Briefly, U266 and MM.1S cells were seeded in six-well plates, and free BTZ, PB, PB@M, and T-PB@M were added with the same concentration of BTZ at 50 nmol·L^{-1}, respectively. After 12 h, the cells were washed three times with PBS and stained with the Annexin V-FITC/PI Apoptosis Detection Kit following the manufacturer's instructions. Subsequently, the cells were analyzed by FCM.

2.12. Western blotting

The expression of apoptosis proteins was evaluated by Western blot analysis. Briefly, U266 cells were seeded in a six-well plate and treated as mentioned previously. After cultured for 24 h, the U266 cells were washed with PBS twice and centrifuged at 1000 r·min^{-1} to collect the cell pellets. Proteins were extracted using a cold Radio Immunoprecipitation Assay buffer with 0.1% protease inhibitor. Electrophoresis was conducted by loading 50 μg of proteins into each well of the SDS-PAGE before transferring the proteins to a polyvinylidene difluoride (PVDF) membrane. The PVDF membrane was then blocked in 5% fat-free milk for 2 h at room temperature and subsequently incubated with primary antibodies against PARP1, Caspase-3, Bcl-2, and glyceraldehyde-3-phosphate dehydrogenase (GAPDH) (as an internal control protein) overnight at 4 °C, respectively. Afterwards, the PVDF membranes were incubated with horseradish peroxidase (HRP)-conjugated secondary antibodies for 2 h at room temperature and the protein bands were visualized using chemiluminescence reagent autoradiography by Gel Imager System.

2.13. Reactive oxygen species (ROS) assay

The generation of ROS induced by free BTZ, PB, PB@M, and T-PB@M treatments in U266 and MM.1S cells were detected by flow cytometry analysis. Firstly, U266 and MM.1S cells were seeded in six-well plates at a density of 1.0×10^6 cells per well in 2.0 mL of medium containing free BTZ, PB, PB@M, and T-PB@M with the same concentration of BTZ at 50 nmol·L^{-1}, and cultured for 24 h. Then the U266 and MM.1S cells were harvested and washed three times with PBS. Subsequently, the cells were stained with DCFH-DA for 30 min at 37 °C in the dark. The fluorescence of the cells was then immediately analyzed by FCM.

2.14. Establishment of MM mice models

The male BALB/C-nu/nu and NCG mice were used to establish the animal models of MM. MM with bone involvement animal model: after anesthetization of the mice, U266 cells (5×10^6 cells in 100 μL RPMI 1640 medium) were injected into the right tibia; orthotopic MM animal model: U266 cells (1×10^7 cells in 100 μL RPMI 1640 medium) were injected into the tail vein.

2.15. In vivo *biodistribution studies*

MM bearing mice were randomly divided into three groups, each containing three mice. IR780-labeled PB, PB@M, and T-PB@M were administrated. The fluorescence intensity of the nanoparticles in the mice was monitored at various time points using the IVIS®Spectrum Imaging System (excitation: 745 nm, emission: 820 nm; PerkinElmer, USA). After that, the mice were sacrificed and the tissues, including the heart, liver, spleen, lung, kidney, tumor bearing hindlimb, and healthy hindlimb, were collected for imaging.

2.16. Safety evaluation and bone affinity studies

The safety evaluation of free BTZ, PB, PB@M, and T-PB@M was conducted by blood biochemistry analysis. ICR male mice were randomly divided into two groups. One group of mice was used for the single-dose toxicity experiments, and the other group was used for the multiple-dose toxicity experiments. The mice in both groups were injected with PBS, free BTZ, PB, PB@M, and T-PB@M at an equivalent BTZ dose of 0.5 mg·kg^{-1} on day 1 (single dose) or on days 1, 3, 5, and 7 (multiple doses). On day 2 (for the single-dose group) and day 8 (for the multiple-dose group), blood samples were collected and centrifuged (1500g, 15 min, 4 °C) to obtain plasma. Serum levels of ALT, AST, BUN, and CREA were measured.

The binding of PB, PB@M, and T-PB@M to the mice tibia and femur were performed. Briefly, IR780-labeled PB, PB@M, and T-PB@M were incubated with the mice tibia and femur *ex vivo* for 2 h and then washed with PBS. The bone affinity was detected by fluorescence intensity using an *in vivo* optical three-dimensional imaging system (IVIS®Spectrum Imaging System) for small animals.

2.17. In vivo *therapeutic efficacy*

MM mice were randomly divided into four groups, each containing five mice. The mice in each group were injected with PBS, free BTZ, PB@M, and T-PB@M at equivalent BTZ doses of 0.5 mg·kg^{-1} on days 1, 3, 5, and 7, respectively. Throughout the experiment, the weight and lifespan of the mice were recorded. On the 28th day, the mice were euthanized, and blood samples were collected and centrifuged (1500g, 15 min, 4 °C) to obtain plasma. Myeloma markers, including hemoglobin, CREA, serum calcium, immunoglobulin G, and urine protein, were tested. The mice bone marrow was collected for bone marrow aspiration, and the heart, liver, spleen, lung, kidney, and other major organs were harvested, fixed in 4% paraformaldehyde, embedded in paraffin, and stained with hematoxylin and eosin (H&E).

2.18. Statistical analysis

All the data in this paper were processed using GraphPad Prism 9.0 Software. The test data were expressed as mean ± standard

deviation (SD). The level of significance was analyzed based on Student's *t*-test: $^{*}p < 0.05$, $^{**}p < 0.01$, $^{***}p < 0.001$.

3. Results and discussion

3.1. Preparation and characterization of T-PB@M

The dual-targeting nanoparticle (T-PB@M) utilized in this study had three main components: a polymeric core with BTZ conjugation, an outer shell derived from MM cell membrane, and a biphosphate functionalized bone-targeting corona. To prepare T-PB@M (Fig. S1 in Appendix A), a star-shape biodegradable polyaspartamide was first synthesized through ROP with G0 PAMAM as an initiator, followed by ammonolysis, as described in a previous report [42]. Subsequently, CA was grafted onto the amino pendants of polyaspartamide. And the success of polyaspartamide and polyaspartamine–CA were confirmed using NMR spectroscopy as shown in Figs. S2 and S3 in Appendix A. Upon loading BTZ, a pH-sensitive covalent borate ester bond was formed between the boric acid group of BTZ and the catechol group of CA, denoted as the drug core portion of this polymer-BTZ conjugation nanoparticle (PB). Thereafter, MM cell membrane vehicles were isolated and coated onto the PB nanoparticles, which resulted in the construction of MM cell membrane-coated PB (PB@M) particles, endowed with homologous targeting functionality. Lastly, the bone-targeting material DSPE–PEG–ALN (Fig. S4 in Appendix A) was introduced into the lipid bilayer of PB@M through hydrophobic interactions, which ultimately yielded the final dual-targeting nanoparticles (T-PB@M).

To optimize the binding affinity of T-PB@M to bone minerals, FITC-labeled T-PB@M formulations with varying ratios of bone-targeting ALN moieties were exposed to incubation with HAP as a representative model component to mimic bone mineral tissue. Through fluorescence intensity measurements on the HAP surface, a gradual increase in signal was observed, indicating an enhanced interaction between T-PB@M and HAP as the ALN content in the formulations increased (Fig. S5 in Appendix A). The fluorescence intensity reached a plateau, however, when the ALN content reached 50%. Beyond this threshold, a lack of significant further fluorescence enhancement was observed even further increasing the ALN content. These results implied that T-PB@M formulations incorporating 50% ALN offered the favorable configuration for bone-targeting nanoparticle, which resulted in a substantial enhancement of the binding affinity to bone minerals.

To verify the successfully preparation of the drug containing nanoparticle, the average size and zeta potential of PB, PB@M, and T-PB@M were determined. As shown in Figs. 2(a) and (b), the PB exhibited an average size of approximately 50 nm. Following the coating of PB with myeloma cell membrane (PB@M), the size increased to around 90 nm, whereas the introduction of DSPE–PEG–ALN into the lipid bilayer of PB@M for T-PB@M led to a size increase of about 120 nm. The zeta potential of the PB nanoparticle was measured to be around 20 mV. Because of the negative charge of the MM cell membrane, this potential reduced to −17 mV for PB@M. In contrast, because of the presence of bone-targeting groups with DSPE–PEG coating on the cell membrane surface, the charge of the T-PB@M nanoparticle was slightly shielded, and the surface charge increased to −13 mV. Additionally, to ascertain the presence of membrane proteins on the surface of T-PB@M nanoparticles for bone marrow targeting, SDS-PAGE analysis was performed (Fig. 2(c)). Consistently with the MM membrane (M), both PB@M and T-PB@M maintained the majority of their associated membrane proteins, which indicated the improved surface performance of T-PB@M. Furthermore, the dispersion stability of the prepared nanoparticles was evaluated using DLS over a seven-day period. As shown in Fig. 2(d), all of the prepared formulations exhibited sustained colloidal stability, which was attributed to the controlled surface charge and the hydrophobic-hydrophilic balance on the particle surfaces. Moreover, transmission electron microscopy (TEM) images revealed the T-PB@M nanoparticles as uniform spherical structures, with each boasting a diameter of approximately 100 nm. Notably, these nanoparticles showed a prominent corona-like coating on their external layer, which was believed to successfully resemble the cell membrane on the surface and which was also observed in PB@M nanoparticles imaging as well (Fig. 2(e)). These observations collectively support the successful preparation of T-PB@M nanoparticles, where their small particle size, appropriate zeta potential, and presence of membrane proteins on the surface established favorable conditions for effective entry into the bone marrow.

3.2. In vitro *hemolysis, drug release, and bone-binding ability assay*

Considering T-PB@M to be a potential clinical therapeutic drug for MM treatment, it is essential to assess its blood compatibility. Therefore, mouse blood compatibility was performed by hemolysis assay to evaluate the cytotoxicity of these hybrids on red blood cells, which were incubated with various prepared formulations at a concentration of 1 $mg{\cdot}mL^{-1}$ of BTZ. As shown in Figs. 3(a) and (b), after 2 h of incubation, PB, PB@M, and T-PB@M showed less than 2% hemolysis, whereas BTZ showed 6% hemolysis against the positive control of pure water. PB, PB@M, and T-PB@M nanoparticles exhibited significantly lower hemolysis rates than BTZ. Besides rabbit blood was also used to the hemolysis assay to verify the biocompatibility of BTZ, PB, PB@M, and T-PB@M. As shown in Fig. S6 in Appendix A, the hemolytic test results of rabbit blood were consistent with that of mouse blood. This observation confirmed the safety and biocompatibility of these formulations, rendering them suitable for potential clinical applications.

The biomimetic nanoparticles in this study were composed of a biodegradable polymeric core, which included polyaspartamine with CA grafting. CA was selected due to its capacity to provide multiple catechol moieties capable of binding and releasing borate-containing BTZ in a pH-dependent manner [43]. It was hypothesized that BTZ dissociated from the core-bound catechol groups under acidic conditions prevailing in cancer tissue or subcellular endosomes, which led to the release of the active drug, thereby exerting its proteasome inhibitory function. To substantiate the validity of this approach, a series of release experiments were conducted under three distinct pH conditions (7.4, 6.5, and 5.0) to emulate the physiological pH found in normal tissues and blood, the acidic extracellular environment of tumors, and the acidic environment within subcellular lysosomes, respectively. As shown in Fig. 3(c), pH-dependent releasing was observed. Under pH = 7.4 (representative of the physiological environment), T-PB@M exhibited negligible release behavior over a 48 h period, indicating the retained relative stability of T-PB@M in the normal physiological milieu without significant drug release. Meanwhile, at pH = 6.5 (representing the tumor extracellular environment), a slightly accelerated release rate was observed. Notably, at pH = 5.0 (simulating the acidic lysosomal environment), the release rate substantially increased, with more than 75% of the drug released within the first 8 h and more than 80% released within 24 h. These results highlighted the pronounced pH dependency of the release rate and quantity, which can be attributed to the formation of characteristic acid-cleavable dynamic covalent bonding within the T-PB@M. Furthermore, the releasing profiles of different formulations (PB, PB@M, and T-PB@M) under the acidic condition (pH = 5.0) were investigated. As shown in Fig. 3(d), PB@M and T-PB@M exhibited relatively slower release rates than PB. This phenomenon may be attributed to the presence of the

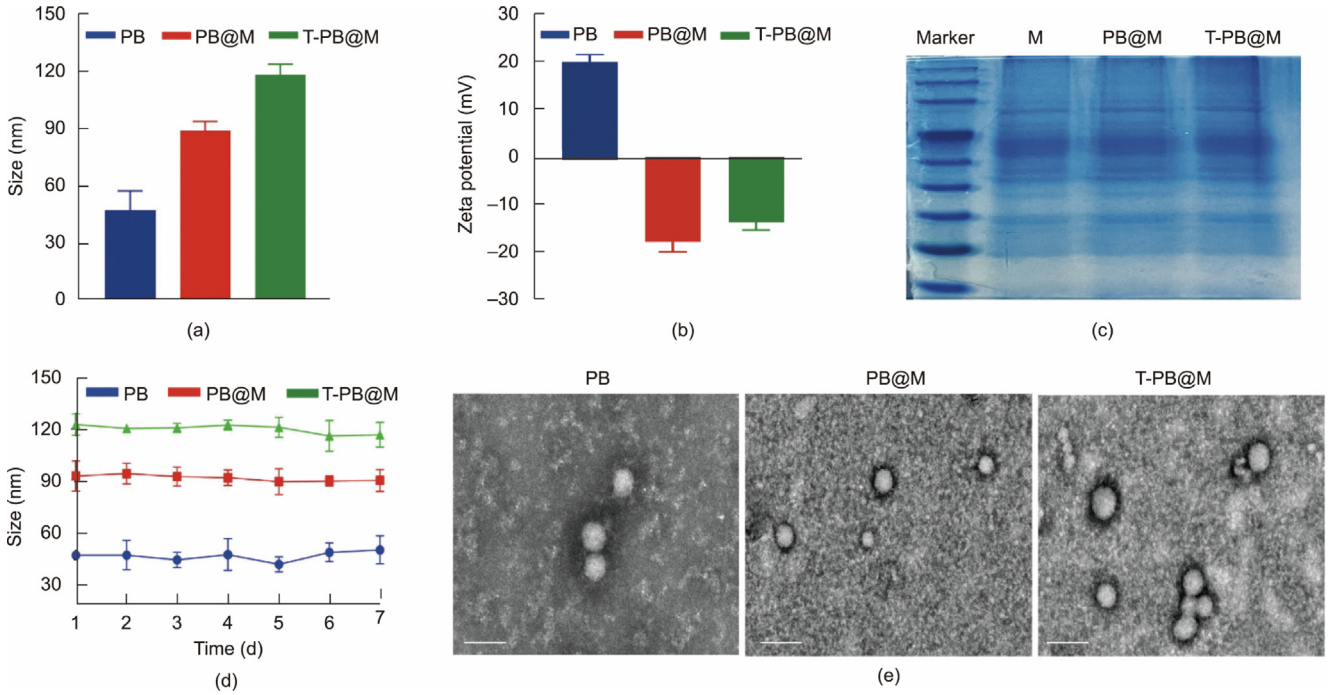

Fig. 2. (a) Size of PB, PB@M, and T-PB@M nanoparticles. (b) Zeta potentials of PB, PB@M, and T-PB@M nanoparticles measured by DLS. (c) SDS-PAGE analysis of the membrane of MM cells and PB@M and T-PB@M nanoparticles. (d) Stability of PB, PB@M, and T-PB@M nanoparticles in PBS for 7 d. (e) TEM images of PB, PB@M, and T-PB@M nanoparticles (scale bar = 100 nm).

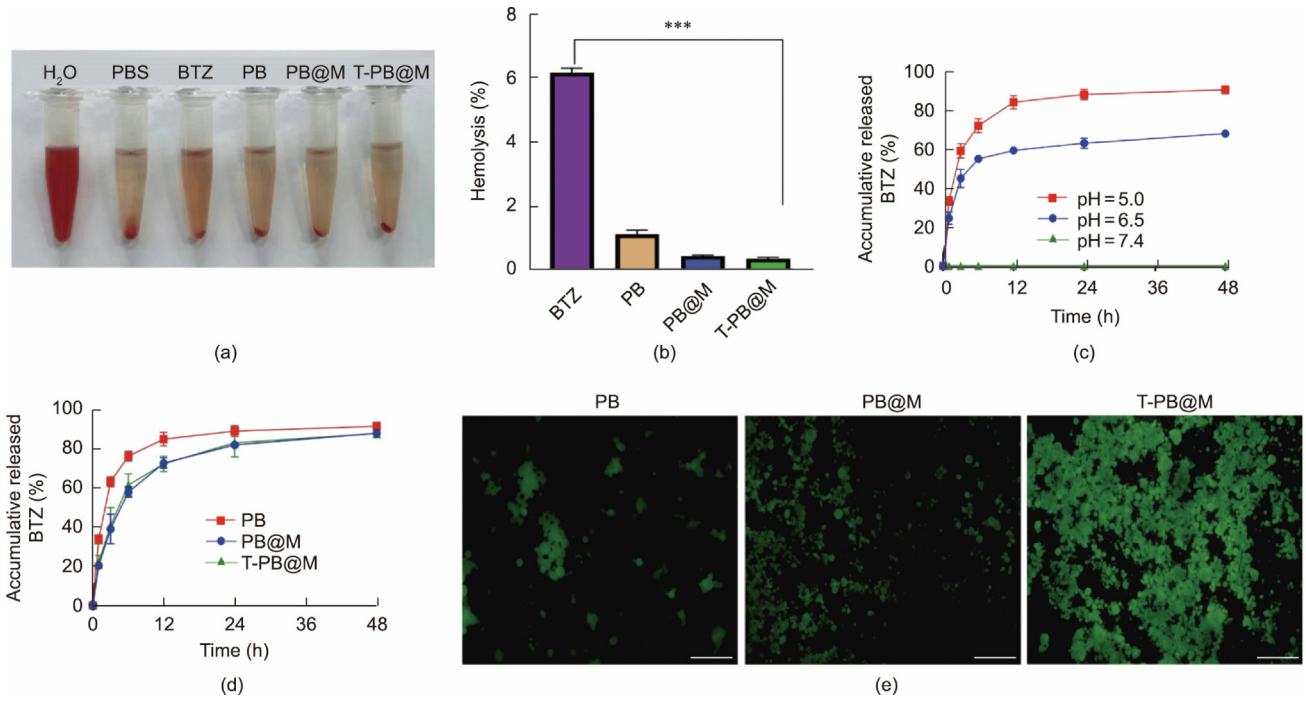

Fig. 3. (a) Picture of the hemolysis experiment with nanoparticles. (b) Hemolysis (%) of BTZ, PB, PB@M, and T-PB@M ($n = 3$, $^{***}p < 0.001$). (c) *In vitro* release profile of T-PB@M in PBS at different pH. (d) *In vitro* release profile of PB, PB@M, and T-PB@M in PBS at pH = 5.0. (e) HAP binding of PB, PB@M, and T-PB@M nanoparticles at room temperature (scale bar = 100 μm).

MM cell membrane shell coating, which hindered the release of the drug from these formulations. Notably, despite the varied release rates, all formulations achieved 80% of drug release within 48 h. This finding suggests that they demonstrated comparable therapeutic efficiency intracellularly, despite differences in their release kinetics. Thus, the dual-targeting nanoparticles exhibited favorable drug release behavior and showed promising potential to enhance the therapeutic effect at the targeted site.

The T-PB@M nanoparticles were developed not only with a pH-sensitive polymeric drug loading core but also a cell membrane-fabricated outer shell consisting of a PEG corona functionalized with ALN moiety. The rationale for incorporating ALN was based

on its demonstrated affinity toward bone tissues. The targeting capability of T-PB@M to the affected bone site holds potential for enhancing the therapeutic efficacy in treating MM while mitigating toxic side effects on other organs. To evaluate the bone tissue binding capacity of T-PB@M nanoparticles, binding assay was conducted using various FITC-labeled formulations incubated with bone tissues to mimic materials (e.g., HAP). As shown in Fig. 3(e) and Fig.S7 in Appendix A, T-PB@M exhibited a notable 4.7- and 3.6-fold higher HAP-binding percentage compared with that of PB and PB@M after 1 h of incubation, respectively. After 6 h of incubation, T-PB@M showed a substantial 90% binding to HAP, whereas PB and PB@M retained a binding level of approximately 20%. These results demonstrated the significantly enhanced bone-targeting ability of T-PB@M in comparison to PB and PB@M in an *in vitro* setting, thereby indicating that the incorporation of ALN effectively conferred bone-targeting functionality to the nanocarrier.

3.3. In vitro *cytotoxicity, cellular uptake, and cell apoptosis studies*

Following the confirmation of the effective bone-targeting ability of T-PB@M, the *in vitro* toxicity of different BTZ-containing formulations compared with BTZ was further assessed using the MTT assay. Typically, various concentrations of PB, PB@M, and T-PB@M were incubated with MM cells (U266 and MM.1S cells) for different time durations. The results revealed that the BTZ formulations elicited cell death in a dose-dependent manner, as shown in Figs. 4(a) and (b) and Fig. S8 in Appendix A. T-PB@M and PB@M both demonstrated significant inhibition of MM cell lines. Especially in the U266 cells, T-PB@M and PB@M exhibited average half-inhibitory concentration (IC_{50}) values of 177 and 200 nmol·L^{-1}, respectively, after 24 h of incubation. These values were similar to that of free BTZ (172 nmol·L^{-1}) but were lower than that of PB (286 nmol·L^{-1}). Furthermore, after 48 h of incubation, T-PB@M and PB@M maintained comparable inhibition efficiency with IC_{50} values of 104 and 108 nmol·L^{-1}, respectively, whereas the IC_{50} values for PB and free BTZ were 125 and 75 nmol·L^{-1}, respectively. These results indicated that cell membrane-coated nanoparticles T-PB@M and PB@M exhibited comparable cytotoxicity against MM cells to the clinical drug BTZ, thereby highlighting the potential of the MM cell membrane coating strategy as a promising therapeutic formulation for the treatment of MM.

To elucidate the reasons for achieving the desired high toxic effects of BTZ delivery through cell membrane-coated nanoparticles, it was essential to investigate their intracellular uptake behavior. For this purpose, FITC was loaded as a fluorescent probe to track the nanoparticles. The labeled nanoparticles were incubated with U266 cells for 4 h, and the relative amount of cellular uptake of nanoparticles was observed by fluorescent microscope and FCM. As shown in Fig. 4(c), after interaction with the cells, the fluorescence intensity of U266 cells treated with the T-PB@M and PB@M nanoparticles was higher than that of the cells treated with the PB nanoparticles. For further quantitative verification, FCM was used for the fluorescence intensity analysis. The mean fluorescence intensity of U266 cells for both T-PB@M group was 1.8-fold higher than that for the PB group (78.5% versus 42.5%), which was comparable to that in the PB@M group (Figs. 4(d) and (e)). These results demonstrated that the cell membrane-coated nanoparticles exhibit enhanced cellular uptake and internalization capabilities, which was likely attributed to the fluidity of the cell membrane and the homologous targeting of membrane proteins. These findings were consistent with the results obtained from the MTT assay, providing further evidence for the improved cytotoxicity of T-PB@M and PB@M nanoparticles against MM cells.

The induction of apoptosis and necrosis on U266 and MM.1S cells induced by various formulations incorporating BTZ was further evaluated by FCM using the Annexin V-FITC/PI Apoptosis Detection Kit. As shown in Figs. 5(a) and (b), the apoptotic rate of U266 of free BTZ was measured at only 33.3%. PB exhibited a higher apoptotic rate treatment, which resulted in a significant increase to 63.0%. Notably, T-PB@M exhibited the most pronounced apoptosis with up to 78.3% of cells undergoing apoptosis, among all tested groups at a specific concentration of 50 nmol·L^{-1} BTZ and after 12 h of incubation. This apoptotic rate was comparable to that observed in the PB@M group, which recorded a value of 71.0%. As shown in Fig. S9 in Appendix A, the apoptotic trend of MM.1S treated with BTZ, PB, PB@M, and T-PB@M was consistent with that of U266. Conversely, the increased apoptotic response observed with T-PB@M and PB@M could be attributed to several key factors. First, the nanosize particles of T-PB@M and PB@M facilitated enhanced internalization into the target cells, increasing drug uptake and bioavailability. Second, the MM cell membrane shell coating provided active targeting capabilities, directing the drug specifically toward the MM cells, thus maximizing its therapeutic effects. Additionally, the drug conjugation within the nanoparticles was sensitive to the acidic intracellular environment. This acid-sensitive conjugation enabled a faster release of the drug within the MM cells, enhancing its cytotoxicity and apoptotic effects. These significant findings highlight the potential of T-PB@M as a promising candidate for BTZ therapy, because it effectively induced apoptosis in MM cells with enhanced cytotoxicity.

To further substantiate the proapoptotic capacity of T-PB@M, an assessment was conducted on the expression levels of various apoptosis-related proteins. PARP1, Caspase-3, and Bcl-2 are significant molecules among these crucial molecules associated with apoptosis regulation [44,45]. PARP1 is an enzyme that plays an important role in the process of apoptosis. PARP1 undergoes hyperactivation, leading to the depletion of vital cellular energy substrates, such as nicotinamide adenine dinucleotide (NAD^+) and adenosine triphosphate (ATP), thereby culminating in apoptosis upon encountering cellular damage. Likewise, Caspase-3, a cysteine aspartic protease, assumes a principal role as the executioner enzyme during apoptosis. Upon the initiation of apoptotic signaling, Caspase-3 is activated, thereby inducing proteolysis within the cellular milieu, eventually leading to cellular demise. In contrast, Bcl-2 functions as an anti-apoptotic protein, significantly affecting apoptosis regulation. It actively inhibits the apoptotic process, providing cellular safeguarding against both intrinsic and extrinsic apoptotic stimuli. Malfunctioning of Bcl-2 has been implicated in the promotion of apoptosis. PARP1 and Caspase-3 undertake complementary roles in the context of cellular damage repair and apoptosis. Additionally, Bcl-2 modulates Caspase-3 activity through the regulation of intracellular apoptotic signaling pathways. Thus, the expression levels of PARP1, Caspase-3, and Bcl-2 in MM cells after treating with BTZ-containing formulations were evaluated. As shown in Fig. 5(c), T-PB@M significantly upregulated the expression of PARP1 and Caspase-3 proteins while concurrently repressing the expression of Bcl-2 protein. These compelling results underscore the heightened capacity of T-PB@M to bolster tumor cell apoptosis, surpassing the performance of free BTZ and PB.

3.4. Intracellular ROS measurement

The excessive production of ROS surpasses the inherent scavenging capacity of the tumor cells, leading to oxidative stress. This phenomenon exerts an anti-tumor effect by inducing apoptosis in the tumor cells. BTZ, a proteasome inhibitor utilized in MM clinical treatment, has recently been found to elevate intracellular ROS levels in addition to its proteasome inhibition function [46,47]. In this context, to investigate the potential mechanism through which T-PB@M promotes apoptosis in tumor cells, an assessment of intracellular ROS levels was conducted. The ROS probe

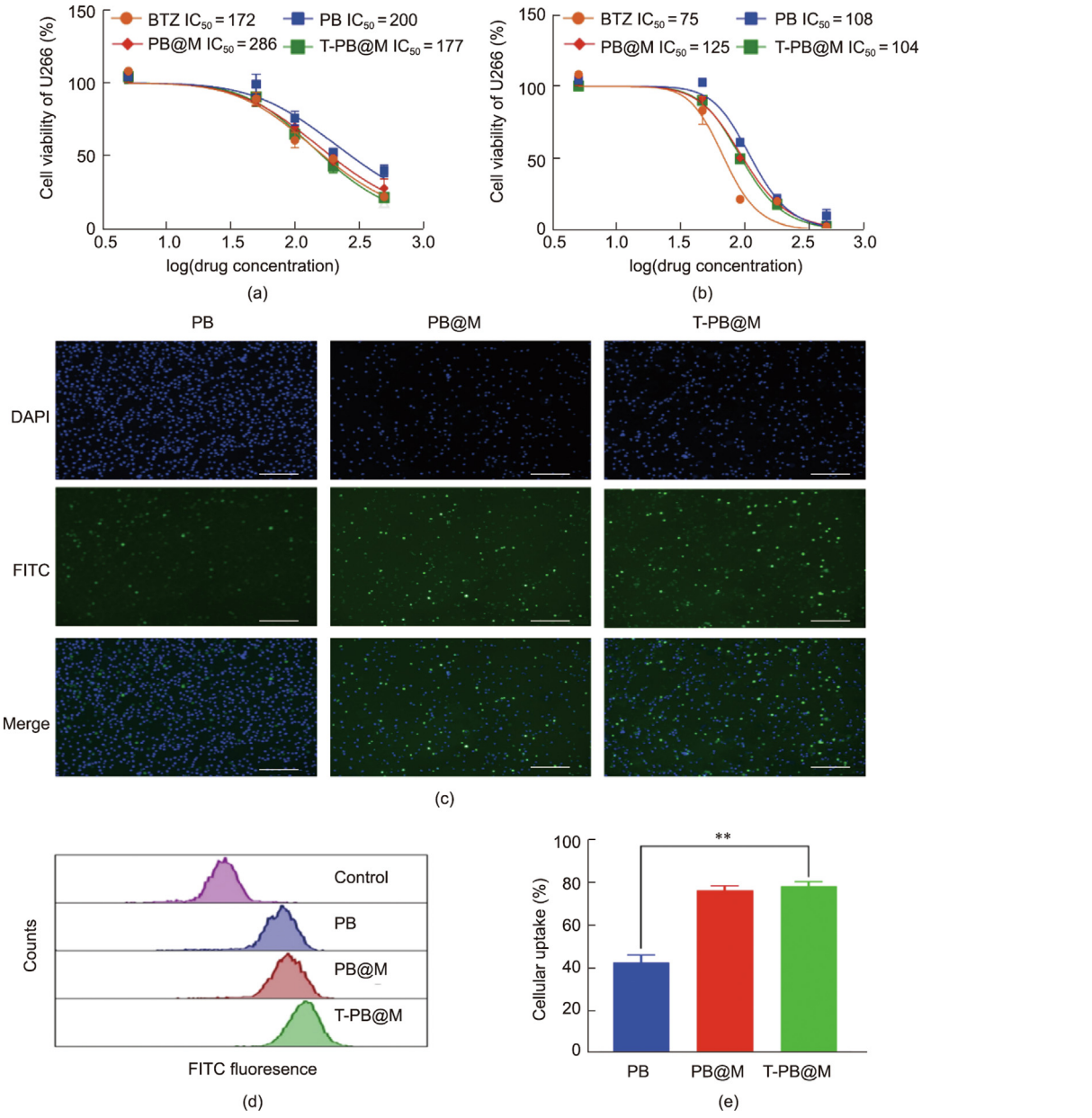

Fig. 4. *In vitro* U266 cytotoxicity of PB, PB@M, and T-PB@M after (a) incubation for 24 and (b) 48 h (the unit for drug concentration is nmol·L^{-1}). The cellular uptake of PB, PB@M, and T-PB@M detected by (c) fluorescent microscope (scale bar = 100 μm) and (d) FCM using FITC as the probe treated for 4 h. (e) Cellular uptake (%) of PB, PB@M, and T-PB@M (n = 3, $^{**}p < 0.01$).

DCFH-DA was employed, and FCM was utilized to detect the production of intracellular ROS. As illustrated in Fig. 5(d) and Fig. S10 in Appendix A, free BTZ and PB exhibited slight increases in ROS levels within 4 h in both U266 and MM.1S cells, whereas PB@M and T-PB@M demonstrated a remarkable surge in ROS production in these MM cells. Particularly, in U266 cells, T-PB@M exhibited an extraordinary effect, causing 90% of the cells to produce ROS. This notable effect may be attributed to the bone marrow microenvironment effects of the cell membrane coating on the nanoparticles, which enabled faster cellular internalization of PB@M and T-PB@M. The results indicated that T-PB@M efficiently generated substantial ROS, thereby eliciting oxidative stress in MM cells and ultimately promoting tumor cell apoptosis. These findings were consistent with the results obtained from the MTT assay, further supporting the notion that the improved cellular uptake and internalization of T-PB@M nanoparticles could contribute to their enhanced cytotoxicity against MM cells. The combination of effective cellular uptake, pH-responsive drug release, and bone-targeting ability demonstrated that this cell membrane-coating strategy is a promising approach for achieving high therapeutic efficacy in the treatment of MM.

3.5. In vivo *biodistribution studies*

To clarify the biological distribution of T-PB@M *in vivo*, MM with bone involvement mice model was established. In order to track the selective accumulation of T-PB@M in bone lesions, IR780 was loaded as a fluorescent probe. In this experiment, IR780-labeled nanoparticles were tail vein injected into MM mice and the fluorescence at different time intervals was monitored. As shown in Fig. 6(a), during the course of the experiment, PB and PB@M were exhibited with little fluorescence intensity

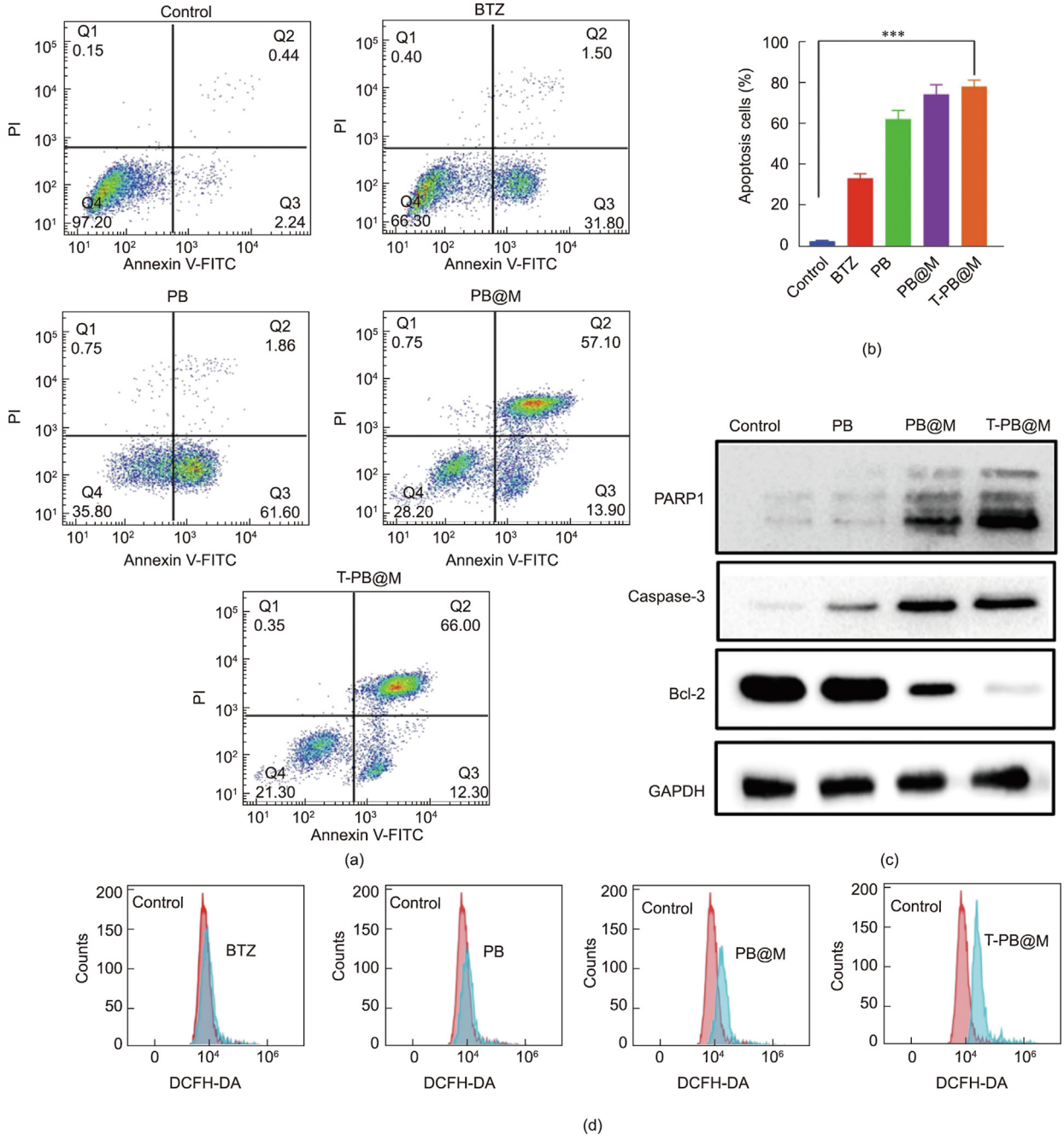

Fig. 5. (a) FCM analysis of U266 cells treated with BTZ, PB, PB@M, and T-PB@M. The cells were stained with Annexin V-FITC and PI for analysis. (b) Apoptosis cell (%) of PB, PB@M, and T-PB@M ($n = 3$, $^{***}p < 0.001$). (c) Western blot analysis of the expression of PARP1, Caspase-3, and Bcl-2 after being treated with PB, PB@M, and T-PB@M. (d) FCM analysis using DCFH-DA as probe after being treated with BTZ, PB, PB@M, and T-PB@M.

observed in the bone. Meanwhile, T-PB@M exhibited a noticeable fluorescence signal at the bone lesion site as early as 2 h post-injection, which then intensified over time.

To substantiate the intravital colocalization of nanoparticles, a subsequent evaluation of *ex vivo* fluorescence intensity was performed across principal organs, encompassing the heart, liver, spleen, lung, and kidney, at the 12-h post-injection time point. Additionally, the non-pathological (left) and pathologically affected (right) hindlimbs were also subject to this analysis. As shown in Figs. 6(b) and (c), PB exhibited its most prominent fluorescence intensity within the liver, a phenomenon denoted as the "first-pass effect," which is rooted in hepatic metabolism dynamics. Nevertheless, the hepatocellular clearance trajectories of PB@M and T-PB@M displayed retardation as a result of the cloaking of the MM cell biomimetic membranes, conferring immune-evasive attributes on the nanoparticles, as previously described [48]. Notably, the most elevated fluorescence intensity within the limb housing bone lesions was noted in the cohorts treated with T-PB@M, surpassing PB and PB@M by more than 4.0- and 1.5-fold, respectively, across all evaluated time points. This escalated intensity in the bone lesions of the T-PB@M group to the active targeting prowess of ALN, which augmented the nanoparticles' specificity for bone locales. Moreover, quantitative scrutiny of bone/liver fluorescence intensity, as illustrated in Fig. 6(d), unveiled a notably 3.0- and 10.0-fold enhancement in bone-to-liver ratios for T-PB@M in comparison with PB@M and PB, respectively. This

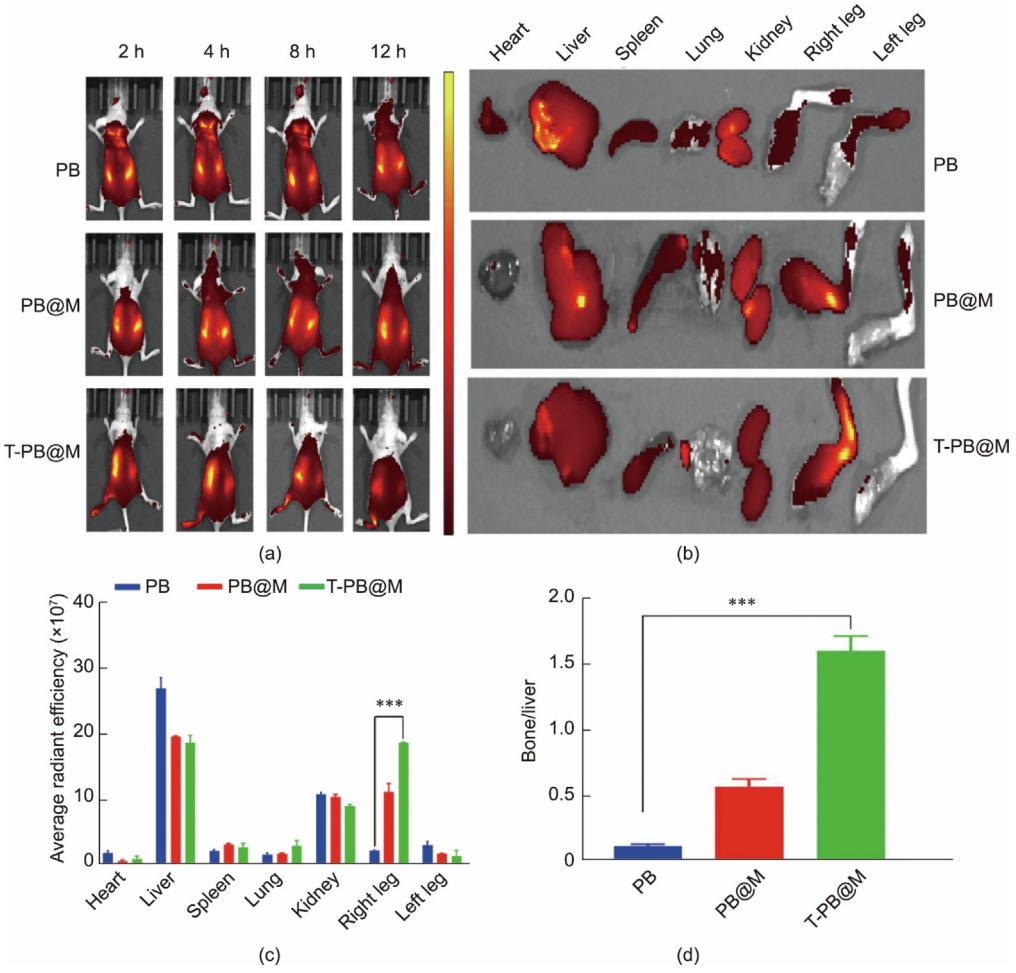

Fig. 6. (a) *In vivo* distribution of PB, PB@M, and T-PB@M in the MM mice using IR780 as probe detected by the IVIS®Spectrum Imaging System. (b) Fluorescence images of main organs after intravenous injection. (c) Quantitative analysis of the mean fluorescence intensity of each organ at 12 h after injection. (d) The ratios of fluorescence intensity of bone/liver (n = 3, $^{***}p < 0.001$).

pronounced enhancement is attributed to T-PB@M's dual-targeting mechanism to the bisphosphate-functionalized bone-targeting corona synergizing with the bone marrow homing effect, which was facilitated by the biomimetic cell membrane coating. These attributes facilitated the preferential accumulation of dual-targeting nanoparticles within the bone marrow upon intravascular administration, concurrently curbing hepatic accumulation. The findings collectively validated the selective sequestration of T-PB@M within the bone lesions, thereby potentially enhancing the therapeutic effectiveness of MM *in vivo*, while also simultaneously addressing concerns related to immune clearance.

3.6. Safety evaluation and bone affinity studies

The assessment of the biocompatibility of nanoparticles was carried out through the examination of blood biochemical markers after single and multiple dosage of varies formulations [49,50]. The indicators of liver function, such as ALT, AST, BUN, and CREA, which served as reflections of kidney function were measured. As shown in Figs. 7(a)–(d), a significant elevation in ALT and AST levels was observed subsequent to the administration of multiple doses of free BTZ, in contrast to other groups, which indicated the induction of hepatic injury and hepatotoxicity in mice. Neither BUN nor CREA, however, exhibited noteworthy changes in response to free BTZ administration, thereby suggesting minimal renal toxicity. Notably, in mice administered with either a single or multiple doses of T-PB@M, there were no substantial variations observed in serum AST, ALT, BUN, or CREA levels, compared with the PBS control group. This phenomenon could be attributed to the synergistic impact of T-PB@M's dual targeting at the lesion sites and the delayed release of chemotherapeutic agents within healthy tissues. Thus, the biosafety outcomes indicated that, relative to free BTZ, the utilization of T-PB@M nanoparticles could ameliorate systemic toxicity and exhibit favorable biocompatibility. Moreover, the bone-targeting efficacy of T-PB@M particles was further substantiated through experimentation involving murine tibia and femur specimens. After two-hour incubation with IR780-labeled PB, PB@M, and T-PB@M, *ex vivo* murine tibia and femur samples were subjected to assessment through IVIS Spectrum. As illustrated in Figs. 7(e) and (f), because of the robust bone-targeting attribute of ALN, the T-PB@M group exhibited an exceptional fluorescence intensity, surpassing that of the PBS group by a notable factor of 10.2-fold. Conversely, the fluorescence intensities of the PB and PB@M groups were comparatively feeble, showing no significant disparities. These findings validated the commendable biocompatibility and limited systemic toxicity profile of T-PB@M, while concurrently accentuating its capability for precise bone targeting for its prospective use in the therapeutic intervention of MM.

3.7. In vivo *therapeutic effect*

MM is an aggressive hematological malignancy frequently marked by clinical indicators including calcium elevation, renal insufficiency, anemia, and bone pain (CRAB criteria). To monitor

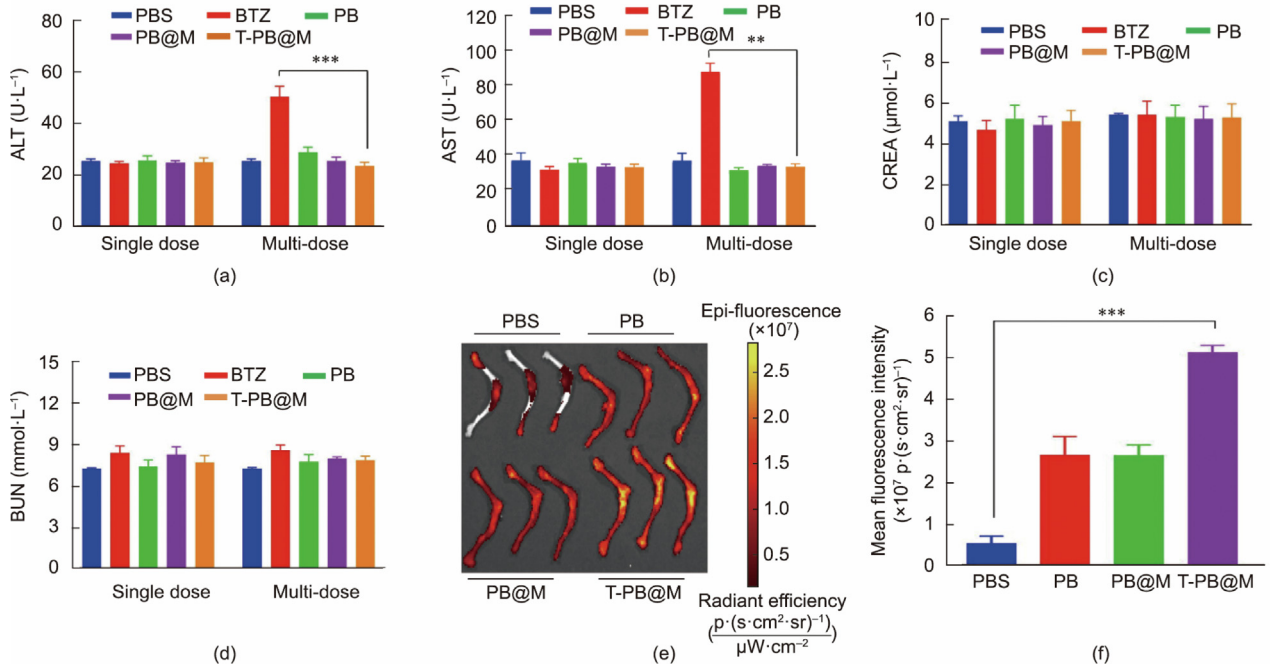

Fig. 7. The detection of blood biochemical indicator, including (a) ALT, (b) AST, (c) CREA, and (d) BUN after one-dose and four-dose injections of PBS, BTZ, PB, PB@M, and T-PB@M (n = 5, $^{**}p < 0.01$, $^{***}p < 0.001$). (e) The affinity of PB, PB@M, and T-PB@M toward the intact *ex vivo* mice tibia and femur detected by the IVIS®Spectrum Imaging System. (f) Quantification of fluorescence intensity at two-hour incubation (n = 3, $^{***}p < 0.001$). p: photons; sr: steradian.

the progression of MM, the comprehensive evaluation encompassing parameters, such as blood hemoglobin levels, serum calcium, immunoglobulin levels, urine protein content, and bone marrow smears related to CRAB were conducted [51–53]. Therefore, an investigation was performed to measure clinical indicators of MM and to assess the effects of T-PB@M therapy on mice with bone-involved disease. As demonstrated in Fig. 8(a), the orthotopic U266 MM model was established through the tail vein injection of U266 cells into NCG mice to evaluate the anti-MM performance *in vivo*. After 14 days of injection, the mice were randomly divided into four groups, which received saline, free BTZ, PB@M, and T-PB@M at the BTZ dose of 0.5 mg·kg^{-1} on days 1, 3, 5, and 7. The mice without injection tumor cells were used as the control. Observations were conducted after four treatments, and the mice were euthanized occurred on day 28. Throughout the experiment, stringent monitoring was implemented for the body weight and survival status of the mice. As shown in Figs. 8(b)–(e), in comparison to saline treatment groups (Mock), T-PB@M therapy resulted in a noticeable increase in hemoglobin levels, a reduction in serum calcium levels, mitigation of proteinuria, and a decrease in serum immunoglobulin production among MM mice. It is worth noting that the dual-targeting T-PB@M exhibited the most substantial amelioration of indicators compare with the PB@M, which resulted in the restoration of the CRAB criteria levels to those of the control group, thereby denoting a commendable antineoplastic efficacy predominantly within the bone marrow. This augmented antitumor effect attributed from the therapeutic agent's dual-targeting proficiency, including not only the bone marrow homing of the tumor cell coating but also the direct bone targeting of the ALN corona. The enhanced antitumor efficacy of T-PB@M was further confirmed through scrutiny of bone marrow smears from MM bearing mice. The MM bearing mice depicted an abundance of blue–purple plasma cells, which indicated the progress of MM. After T-PB@M treatment, the plasma cell abundance within the bone marrow exhibited negligible divergence compared with healthy counterparts (Fig. 8(f)). These outcomes have substantiated the effectiveness of the strategy of engineering dual-targeting properties within nanoparticles, addressing both bone marrow targeting and bone microenvironment homing. In this case, BTZ was delivered into the bone lesion and subsequently accumulated in the MM site, thereby enhancing the therapeutic efficacy against MM.

Moreover, the daily records meticulously tracked survival rates and changes in body weight. As illustrated in Figs. 9(a) and (b), mice subjected to BTZ treatment exhibited pronounced reduction in weight and rapid mortality, which was ostensibly attributed to the inherent toxicity of BTZ. In contrast, MM bearing mice showed marginal weight loss and a prolonged survival rate following administration of T-PB@M, when compared with the control groups (Mock and BTZ cohorts). Moreover, a comprehensive evaluation of major organ histology was performed using H&E staining. As shown in Fig. 9(c), the Mock group exhibited discernible organ dysfunction in comparison to the control group (healthy mice). After being treated with free BTZ, significant cardiotoxic and hepatotoxic effects were conspicuously observed in the BTZ-treated groups, which were directly attributable to their toxicity and induced mortality. Conversely, following treatment with T-PB@M and PB@M, organ functionality was effectively restored to a normal state, with no discernible pathological changes observed in the primary organs of the T-PB@M group, mirroring the condition of normal mice. Remarkably, T-PB@M nanoparticles played a pivotal role in enhancing the overall survival rate, mitigating systemic adverse effects, and notably demonstrating an absence of histological toxicity across all examined organs. These compelling results provide strong evidence not only for the safety but also for the remarkable therapeutic potential of T-PB@M nanoparticles in the context of treating MM.

4. Conclusion

In this study, a dual-targeting nanoparticle (T-PB@M) was developed for the treatment of MM, a plasma cell malignancy.

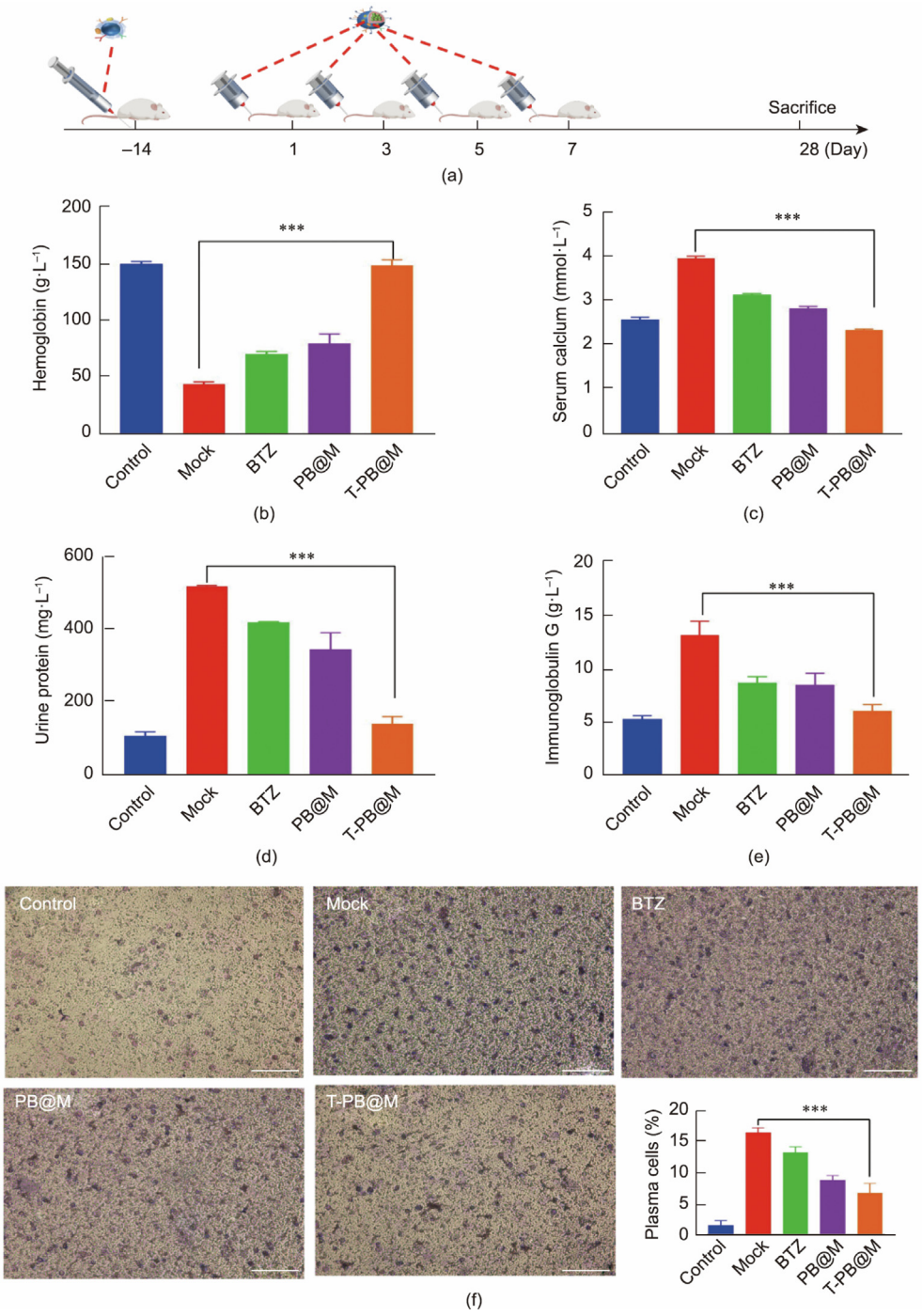

Fig. 8. (a) Diagram showing how the U266 orthotopic model and its method of treatment were established. The detection of blood biochemical indicator, including (b) hemoglobin, (c) serum calcium, (d) urine protein, and (e) immunoglobulin G levels after treated with BTZ, PB@M, and T-PB@M (n = 6, ***p < 0.001). (f) Bone marrow smear images after treated with PB, PB@M, and T-PB@M (scale bar = 100 μm; n = 3, ***p < 0.001).

The T-PB@M nanoparticle system combined several key components to enhance its therapeutic efficacy. This approach consisted of a polymeric core linked to the anti-MM drug BTZ through a pH-responsive linkage, an outer layer derived from MM cell membranes that facilitated BMH, and a bone-targeting corona functionalized with biphosphate groups. This innovative design allowed T-PB@M to achieve the controlled release of chemotherapeutic BTZ specifically within the low-pH microenvironment of the tumor cells. Notably, these results demonstrated the exceptional dual-targeting precision of T-PB@M, enabling it to effectively home in on intraosseous HAP and bone marrow regions, where MM cells reside, because of the presence of specific proteins on the MM cell membrane. Beyond targeting, T-PB@M induced the generation of ROS within MM cells, hindering their growth and viability. This effect was orchestrated through the upregulation of PARP1 and Caspase-3 proteins, coupled with the downregulation of the anti-apoptotic Bcl-2 protein, ultimately driving MM

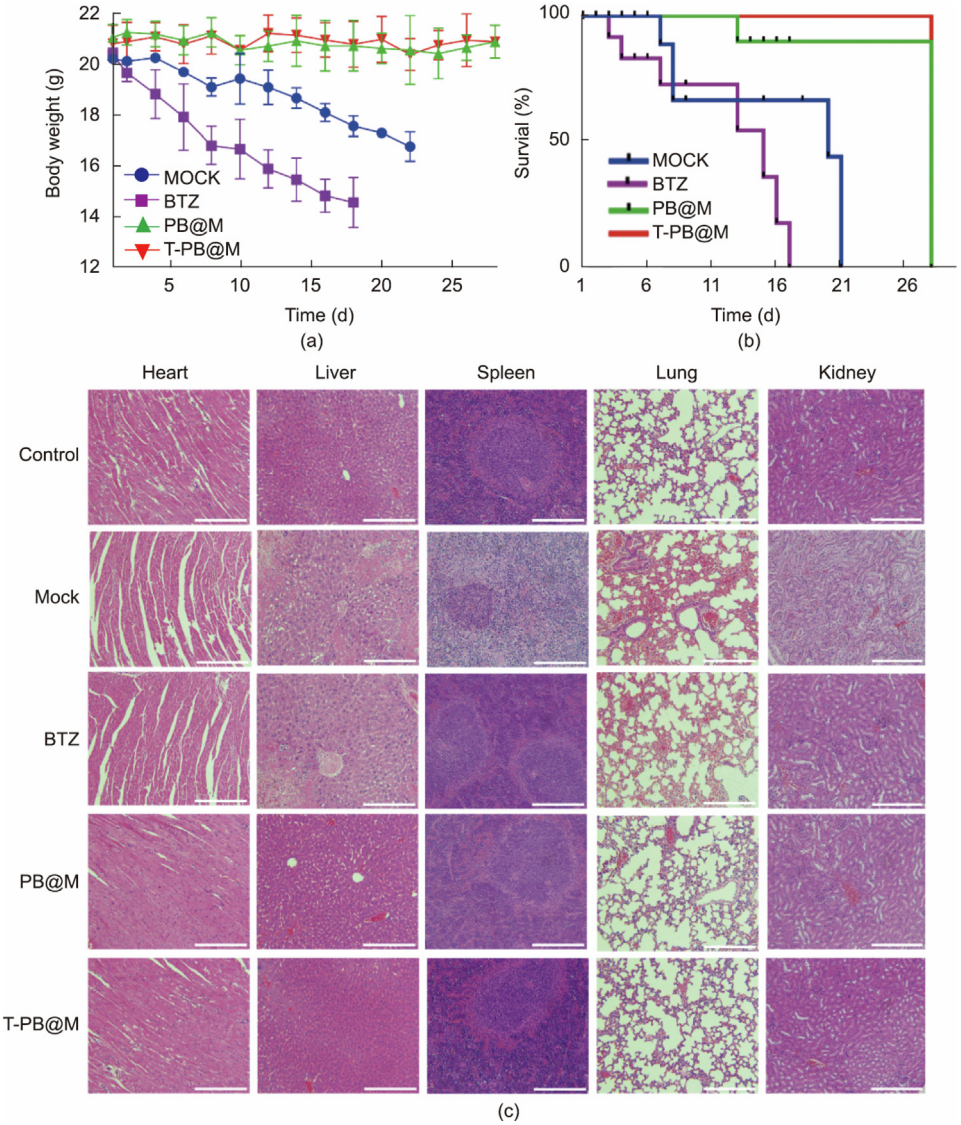

Fig. 9. After treatment with BTZ, PB@M, and T-PB@M, MM mice changes in (a) body weight, (b) survival curves (n = 6), and (c) H&E images of major organs (scale bar = 100 μm).

cell apoptosis. Importantly, the dual-targeting nature of T-PB@M enhanced its specific delivery to bone lesions and subsequent accumulation at MM sites, which led to the controlled release of BTZ, curbing more effective tumor growth, restoring crucial clinical indicators (CRAB), and prolonging survival in an MM mouse model compared with the PB@M. These findings underscore the immense potential of our engineered dual-targeting nanoparticle strategy as an innovative platform for the precise and effective treatment of MM, offering new hope for patients with this challenging malignancy.

Acknowledgments

This research was supported by the National Natural Science Foundation of China (52073145, 82004081); the Jiangsu Talent Professor Program, Jiangsu Innovation Project of Graduate Student (KYCX23-2192); the National Natural Science Foundation of Nanjing University of Chinese Medicine (NZY82004081); the Special Grants of China Postdoctoral Science Foundation (2021T140792). The authors would like to thank Zuoxiu Tie from College of Engineering and Applied Sciences, Nanjing University for the assistance of the IVIS®Spectrum Imaging System.

Authors contribution

Shanshan Wang and Ruogu Qi: conceptualization; Shanshan Wang, Jiayi Yu, Tianming Lu, and Zhiqiang Bi: data curation; Hao Yang, Wenli Lu, and Weibo Liu: formal analysis; Ruogu Qi, Yuanyuan Guo, and Shanshan Wang: funding acquisition; Shanshan Wang, Tianming Lu, and Zhiqiang Bi: visualization; Shanshan Wang and Ruogu Qi: writing—original draft; Ting Niu, Qiang Zhang, and Jun Li: methodology; Yanlin Xin and Zejuan Xie: investigation; Yuanyuan Guo, Yong Bian, and Wenhao Hu: supervision; Ruogu Qi: writing—revised manuscript and editing. All authors have read and agreed to the published version of the manuscript.

Compliance with ethics guidelines

Ruogu Qi, Shanshan Wang, Jiayi Yu, Tianming Lu, Zhiqiang Bi, Weibo Liu, Yuanyuan Guo, Yong Bian, Jianliang Shen, Xuesong Zhang, and Wenhao Hu declare no conflict of interest.

The funders had no role in the design of the study; in the collection, analyses, or interpretation of data; in the writing of the manuscript, or in the decision to publish the results.

Appendix A. Supplementary data

Supplementary data to this article can be found online at https://doi.org/10.1016/j.eng.2024.01.001.

References

[1] Dao A, McDonald MM, Savage PB, Little DG, Schindeler A. Preventing osteolytic lesions and osteomyelitis in multiple myeloma. J Bone Oncol 2022;37:100460.
[2] Makhani SS, Shively D, Castro G, Rodriguez de la Vega P, Barengo NC. Association of insurance disparities and survival in adults with multiple myeloma: a non-concurrent cohort study. Leuk Res 2021;104:106542.
[3] Morris EV, Edwards CM. Bone marrow adiposity and multiple myeloma. Bone 2019;118:42–6.
[4] Ghobrial IM, Detappe A, Anderson KC, Steensma DP. The bone-marrow niche in MDS and MGUS: implications for AML and MM. Nat Rev Clin Oncol 2018;15(4):219–33.
[5] Bommert K, Bargou RC, Stühmer T. Signalling and survival pathways in multiple myeloma. Eur J Cancer 2006;42(11):1574–80.
[6] Joshua DE, Bryant C, Dix C, Gibson J, Ho J. Biology and therapy of multiple myeloma. Med J Aust 2019;210(8):375–80.
[7] Bladé J, Rosiñol L. Complications of multiple myeloma. Hematol Oncol Clin North Am 2007;21(6):1231–46.
[8] Novosad O, Rudiuk T, Shevchuk L, Kundina V, Schmidt A. Outcome of clinical experience of introducing a patient with secondary systemic AL-amyloidosis associated with multiple myeloma. Carcinogenesis 2023;44(1):46–53.
[9] Andrei M, Wang JC. Cutaneous light chain amyloidosis with multiple myeloma: a concise review. Hematol Oncol Stem Cell Ther 2019;12(2):71–81.
[10] Swamydas M, Murphy EV, Ignatz-Hoover JJ, Malek E, Driscoll JJ. Deciphering mechanisms of immune escape to inform immunotherapeutic strategies in multiple myeloma. J Hematol Oncol 2022;15(1):17.
[11] Yang Y, Li Y, Gu H, Dong M, Cai Z. Emerging agents and regimens for multiple myeloma. J Hematol Oncol 2020;13(1):150.
[12] Ri M. Mechanism of action and determinants of sensitivity to the proteasome inhibitor bortezomib in multiple myeloma therapy. Rinsho Ketsueki 2016;57(5):537–45.
[13] Chen W, Yang Y, Chen Y, Du F, Zhan H. Cost-effectiveness of bortezomib for multiple myeloma: a systematic review. Clinicoecon Outcomes Res 2016;8:137–51.
[14] Chen D, Frezza M, Schmitt S, Kanwar J, Dou QP. Bortezomib as the first proteasome inhibitor anticancer drug: current status and future perspectives. Curr Cancer Drug Targets 2011;11(3):239–53.
[15] Liu J, Zhao R, Jiang X, Li Z, Zhang B. Progress on the application of bortezomib and bortezomib-based nanoformulations. Biomolecules 2021;12(1):51.
[16] Qu J, Hou Y, Chen Q, Chen J, Li Y, Zhang E, et al. RNA demethylase ALKBH5 promotes tumorigenesis in multiple myeloma via TRAF1-mediated activation of NF-κB and MAPK signaling pathways. Oncogene 2022;41(3):400–13.
[17] Dou R, Qian J, Wu W, Zhang Y, Yuan Y, Guo M, et al. Suppression of steroid 5α-reductase type I promotes cellular apoptosis and autophagy via PI3K/Akt/mTOR pathway in multiple myeloma. Cell Death Dis 2021;12(2):206.
[18] Wu D, Zhang W, Chen Y, Ma H, Wang M. Platycodin D inhibits proliferation, migration and induces chemosensitization through inactivation of the NF-κB and JAK2/STAT3 pathways in multiple myeloma cells. Clin Exp Pharmacol Physiol 2019;46(12):1194–200.
[19] Ye Z, Chen J, Xuan Z, Yang W, Chen J. Subcutaneous bortezomib might be standard of care for patients with multiple myeloma: a systematic review and meta-analysis. Drug Des Devel Ther 2019;13:1707–16.
[20] Sharp PS, Stylianou M, Arellano LM, Neves JC, Gravagnuolo AM, Dodd A, et al. Graphene oxide nanoscale platform enhances the anti-cancer properties of bortezomib in glioblastoma models. Adv Healthc Mater 2023;12(3):2201968.
[21] Cao Z, Li P, Li Y, Zhang M, Hao M, Li W, et al. Encapsulation of nano-bortezomib in apoptotic stem cell-derived vesicles for the treatment of multiple myeloma. Small 2023;19(40):2301748.
[22] Wang R, Xu X, Li D, Zhang W, Shi X, Xu H, et al. Smart pH-responsive polyhydralazine/bortezomib nanoparticles for remodeling tumor microenvironment and enhancing chemotherapy. Biomaterials 2022;288:121737.
[23] Karges J. Encapsulation of Ru (II) polypyridine complexes for tumor-targeted anticancer therapy. BME Front 2023;4:0024.
[24] Zhang H, Dong S, Li Z, Feng X, Xu W, Tulinao CMS, et al. Biointer face engineering nanoplatforms for cancer-targeted drug delivery. Asian J Pharm Sci 2020;15(4):397–415.
[25] Khan RU, Shao J, Liao JY, Qian L. pH-triggered cancer-targeting polymers: from extracellular accumulation to intracellular release. Nano Res 2023;16(4):5155–68.
[26] Deshantri AK, Varela Moreira A, Ecker V, Mandhane SN, Schiffelers RM, Buchner M, et al. Nanomedicines for the treatment of hematological malignancies. J Control Release 2018;287:194–215.
[27] Huang X, Mahmudul HM, Li Z, Deng X, Su X, Xiao Z, et al. Noble metal nanomaterials for the diagnosis and treatment of hematological malignancies. Front Biosci 2022;27(2):40.
[28] Fang RH, Gao W, Zhang L. Targeting drugs to tumours using cell membrane-coated nanoparticles. Nat Rev Clin Oncol 2023;20(1):33–48.
[29] Gong P, Wang Y, Zhang P, Yang Z, Deng W, Sun Z, et al. Immunocyte membrane-coated nanoparticles for cancer immunotherapy. Cancers 2020;13(1):77.
[30] Zhao X, Yan C. Research progress of cell membrane biomimetic nanoparticles for tumor therapy. Nanoscale Res Lett 2022;17(1):36.
[31] Caocci G, Greco M, La Nasa G. Bone marrow homing and engraftment defects of human hematopoietic stem and progenitor cells. Mediterr J Hematol Infect Dis 2017;9(1):2017032.
[32] Qu Y, Chu B, Wei X, Chen Y, Yang Y, Hu D, et al. Cancer-cell-biomimetic nanoparticles for targeted therapy of multiple myeloma based on bone marrow homing. Adv Mater 2022;34(46):2107883.
[33] Mbese Z, Aderibigbe BA. Bisphosphonate-based conjugates and derivatives as potential therapeutic agents in osteoporosis, bone cancer and metastatic bone cancer. Int J Mol Sci 2021;22(13):6869.
[34] Jing C, Li B, Tan H, Zhang C, Liang H, Na H, et al. Alendronate-decorated nanoparticles as bone-targeted alendronate carriers for potential osteoporosis treatment. ACS Appl Bio Mater 2021;4(6):4907–16.
[35] Klara J, Lewandowska-Łańcucka J. How efficient are alendronate-nano/biomaterial combinations for anti-osteoporosis therapy? An evidence-based review of the literature. Int J Nanomedicine 2022;17:6065–94.
[36] Xi Y, Wang W, Ma L, Xu N, Shi C, Xu G, et al. Alendronate modified mPEG-PLGA nano-micelle drug delivery system loaded with astragaloside has anti-osteoporotic effect in rats. Drug Deliv 2022;29(1):2386–402.
[37] Laconde G, Amblard M, Martinez J. Synthesis of α-amino acid N-carboxyanhydrides. Org Lett 2021;23(16):6412–646.
[38] Kotha S, Meshram M, Panguluri NR, Shah VR, Todeti S, Shirbhate ME. Synthetic approaches to star-shaped molecules with 1,3,5-trisubstituted aromatic cores. Chem Asian J 2019;14(9):1356–403.
[39] Alves CG, de Melo-Diogo D, Lima-Sousa R, Correia IJ. IR780 loaded sulfobetaine methacrylate-functionalized albumin nanoparticles aimed for enhanced breast cancer phototherapy. Int J Pharm 2020;582:119346.
[40] Chen J, Jiang Z, Zhang YS, Ding J, Chen X. Smart transformable nanoparticles for enhanced tumor theranostics. Appl Phys Rev 2021;8(4):041321.
[41] Chan WCW. Principles of nanoparticle delivery to solid tumors. BME Front 2023;4:0016.
[42] Diab HM, Abdelmoniem AM, Shaaban MR, Abdelhamid IA, Elwahy AHM. An overview on synthetic strategies for the construction of star-shaped molecules. RSC Adv 2019;9(29):16606–82.
[43] Ma Y, Li X, Cai L, Li J. pH-Sensitive ε-polylysine/polyaspartic acid/zein nanofiber membranes for the targeted release of polyphenols. Food Funct 2022;13(12):6792–801.
[44] Luanpitpong S, Janan M, Yosudjai J, Poohadsuan J, Chanvorachote P, Issaragrisil S. Bcl-2 family members Bcl-xL and bax cooperatively contribute to bortezomib resistance in mantle cell lymphoma. Int J Mol Sci 2022;23(22):14474.
[45] Xu X, Lin Y, Zeng X, Yang C, Duan S, Ding L, et al. PARP1 might substitute HSF1 to reactivate latent HIV-1 by binding to heat shock element. Cells 2022;11(15):2331.
[46] Pérez-Galán P, Roué G, Villamor N, Montserrat E, Campo E, Colomer D. The proteasome inhibitor bortezomib induces apoptosis in mantle-cell lymphoma through generation of ROS and Noxa activation independent of p53 status. Blood 2006;107(1):257–64.
[47] Zheng Y, Han Y, Sun Q, Li Z. Harnessing anti-tumor and tumor-tropism functions of macrophages via nanotechnology for tumor immunotherapy. Exploration 2022;2(3):20210166.
[48] Paterno F, Shiller M, Tillery G, O'Leary JG, Susskind B, Trotter J, et al. Bortezomib for acute antibody-mediated rejection in liver transplantation. Am J Transplant 2012;12(9):2526–31.
[49] Zelepukin IV, Popov AA, Shipunova VO, Tikhonowski GV, Mirkasymov AB, Popova-Kuznetsova EA, et al. Laser-synthesized TiN nanoparticles for biomedical applications: evaluation of safety, biodistribution and pharmacokinetics. Mater Sci Eng C Mater Biol Appl 2021;120:111717.
[50] You X, Wang L, Zhang J, Tong T, Dai C, Chen C, et al. Effects of polymer molecular weight on *in vitro* and *in vivo* performance of nanoparticle drug carriers for lymphoma therapy. Chin Chem Lett 2023;34(4):107720.
[51] Joshua DE, Bryant C, Dix C, Gibson J, Ho J. Biology and therapy of multiple myeloma. Med J Aust 2019;210(8):375–80.
[52] Ormond Filho AG, Carneiro BC, Pastore D, Silva IP, Yamashita SR, Consolo FD, et al. Whole-body imaging of multiple myeloma: diagnostic criteria. Radiographics 2019;39(4):1077–97.
[53] Chakraborty R, Majhail NS. Treatment and disease-related complications in multiple myeloma: implications for survivorship. Am J Hematol 2020;95(6):672–90.